Composites: Part A 177 (2024) 107958

Contents lists available at ScienceDirect

Composites Part A

journal homepage: www.elsevier.com/locate/compositesa

Book reviews

Modeling anisotropic friction in triaxial overbraiding simulations

A.N. Vu *, W.J.B. Grouve, L.L. Warnet, R. Akkerman

Department of Mechanics of Solids, Surfaces and Systems, University of Twente, P.O. Box 217, NL-7500 AE Enschede, The Netherlands

ARTICLE INFO

Keywords:
B. braiding
B. anisotropy
A. yarn
E. friction

ABSTRACT

Triaxial overbraiding is a highly intricate textile manufacturing process that involves interlacing yarns in three directions, enhancing reinforcement of the final composite compared to biaxial braids. Predictive process simulation is a cost-effective approach to optimizing the manufacturing process. Previous research on biaxial overbraiding simulations indicates that yarn–yarn friction has a significant effect on the braid angle and convergence zone length. This study presents an extended yarn interaction model; it utilizes a fast frontal approach and a Eulerian on Lagrangian method to simulate the complex interlacing of multiple yarns in triaxial overbraiding, including yarn–yarn and yarn–ring friction. Experiments were conducted to evaluate the effect of UD yarn tension on the convergence zone length and braid angle, and to validate the simulations. The model validation shows that a recently proposed anisotropic yarn–yarn friction model predicts braid angle more accurately than an isotropic friction model.

1. Introduction

Overbraiding processes are extensively used for the production of hollow preforms for composite applications [1], owing to their high fiber deposition rates and automation capabilities [2,3]. The interlaced structures these processes produce create braids that can cover complex mandrel shapes while minimizing crack growth and delamination. These attributes make the braids well suited for high volume components that demand superior impact performance [4]. Overbraiding has been successfully applied in the production of various composite components, including rocket motor cases and pressure vessels [5,6]. Biaxial braids are composed of two sets of yarns [7–12]; comparatively, in triaxial overbraiding, a unidirectional (UD) yarn group is added, interlaced with the biaxial yarns, to provide additional advantages, such as increased strength and bending stiffness [13].

Overbraiding manufacturing processes often require several iterations to meet design requirements. This results in expensive trial-and-error procedures and potential tool reworking. Predictive simulation tools enable the manufacturing process to be virtually optimized, minimizing the need for iterative processes and overall costs. This study aims to develop an efficient simulation tool for the triaxial overbraiding process fast enough for design purposes and capable of accurately predicting process outcomes.

1.1. Description of the triaxial overbraiding process

Fig. 1 presents a triaxial overbraiding setup that uses a circle of horn gears. The warp and weft spools are attached to the carriers, which rotate counterclockwise and clockwise, respectively, with the same angular spool velocity $\pm\omega$. The UD spools remain fixed at the center of the horn gear. To accommodate for fluctuations in yarn lengths that occur as a result of shifts in the radial spool position, a tensioning system of springs is utilized for each spool; this is done to maintain consistent yarn tension as described in [6,13,14]. The yarns are guided through a guiding ring and attached to one end of the mandrel. As the warp and weft spools rotate, the yarns interlace with each other. Concurrently, the mandrel is moved through the guide ring at a take-up speed v. The pattern of the braid is achieved through the interlacement of the biaxial yarns. It is common for both biaxial and triaxial overbraiding to employ a regular pattern or 2×2 twill [6].

The position where the yarn touches the mandrel is referred to as the ‘fell point’. The distance from this point to the guide ring is referred to as the ‘convergence zone length’, denoted as H. The ‘braided length’, denoted as L, is the distance from the starting tip of the mandrel to the fell point. Additionally, the braid angle α is determined as the angle between the centerline of the mandrel and the warp or weft yarns.

1.2. Motivation and approach

This section provides an overview of various methods employed for predicting the outcomes of the triaxial overbraiding process. It includes classical analytical models as well as more advanced and realistic approaches.

* Corresponding author.
E-mail addresses: a.n.vu@utwente.nl (A.N. Vu), r.akkerman@utwente.nl (R. Akkerman).

https://doi.org/10.1016/j.compositesa.2023.107958
Received 30 September 2023; Received in revised form 7 December 2023; Accepted 8 December 2023
Available online 15 December 2023

Nomenclature

Vectors:

F	force vector
u	unit vector
n	normal vector
t	tangent vector
e	basis vector
i, j, k	ring coordinate system
r	array of residual coordinate
A, B, C, R	point coordinate vector

Sub and superscripts:

$(*)_m$	denoted for mandrel
$(*)_r$	denoted for guide ring
$(*)_y$	denoted for yarn
$(*)_X$	warp direction
$(*)_O$	weft direction
$(*)_{U/ud}$	uniaxial-direction
$(*)^{int}$	internal indication
$(*)^{ext}$	external indication
$(*)^C$	for yarn-yarn contact
$(*)^t$	tangential component
$(*)^n$	normal component

Scalars:

v	take-up speed
ω	spool angular velocity
L	braided length
H	convergence zone length
r_r	guide ring radius
α	braid angle
φ	inter-yarn angle
μ	coefficient of friction
F	yarn tension
λ	damping factor
ε	convergence criterion
Ψ	slipping function
f	friction force function
k_{90}	orthogonal friction coefficient
n_k	exponential parameter 1
n_n	exponential parameter 2

Operators:

$\|*\|$	Euclidean norm
$(*)\cdot(*)$	scalar product
$(*)\times(*)$	cross product

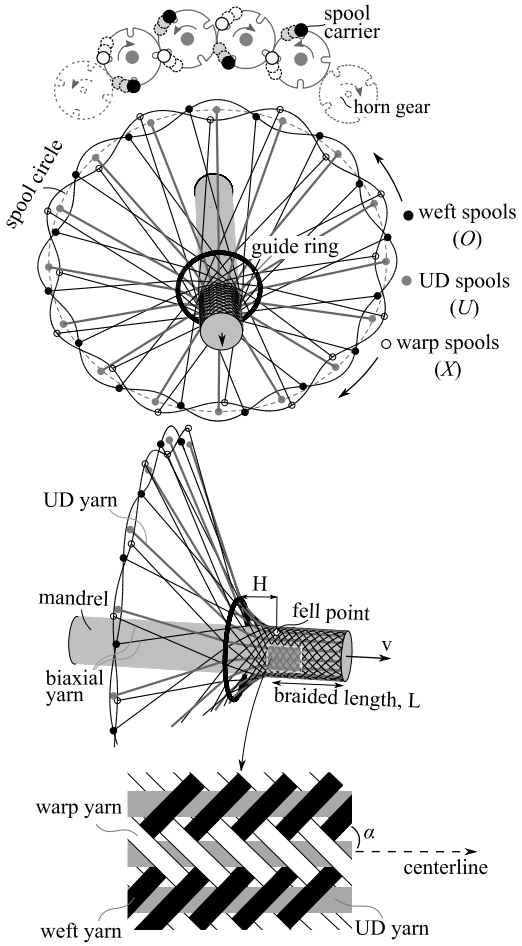

Fig. 1. Schematic illustration of triaxial overbraiding process and a regular pattern of the braid.

The steady state convergence zone length H and braid angle α in triaxial and biaxial overbraiding can be calculated for circular guide rings and mandrels. These parameters are determined as a function of the take-up speed v and the angular spool velocity ω, as described in [15,16]:

$$H = \frac{\sqrt{r_r^2 - r_m^2}}{\tan\alpha} \quad \text{and} \quad \alpha = \arctan\left(\frac{P_m \omega}{2\pi v}\right), \tag{1}$$

where the constants r_r and r_m denote the radius of the guide ring and the circular cross-section of the mandrel, respectively, whereas P_m is the perimeter of the mandrel's cross-section. Despite their computational efficiency, these analytical equations are restricted to simple mandrel geometries and cannot capture the intricate effects of the actual triaxial overbraiding process, including complex yarn–yarn and yarn–ring interactions, yarn deformation and yarn tension variations along the circumference and length of the component.

The Finite Element (FE) method has been employed in several studies for simulating the triaxial overbraiding process [17–20]. This approach facilitates the incorporation of important process features, such as yarn interactions, yarn deformations, and post-deposition slip of yarns. However, the increase of computational complexities required for these simulations is a noteworthy drawback when using such methods for design iterations.

Previously, a so-called 'kinematic model' was introduced [7] to simulate the triaxial overbraiding process [8]. This model offers fast computation but neglects yarn interactions, resulting in less accurate model predictions [8,10,11]. Notably, tensions in the UD yarns affect the convergence zone length and braid angle, as observed experimentally [8]. Previous studies that considered yarn–yarn interactions for biaxial overbraiding [9,12] indicated that the friction between yarns also affects the braid angle and convergence zone length in the unsteady state region. The numerical results show that higher yarn–yarn friction coefficient leads to a lower initial braid angle and a shorter convergence zone length at the steady state, which can be attributed to reduced slippage between the yarns. This effect is even more significant for triaxial overbraiding due to the large number of additional contact points and the presence of UD yarn tension.

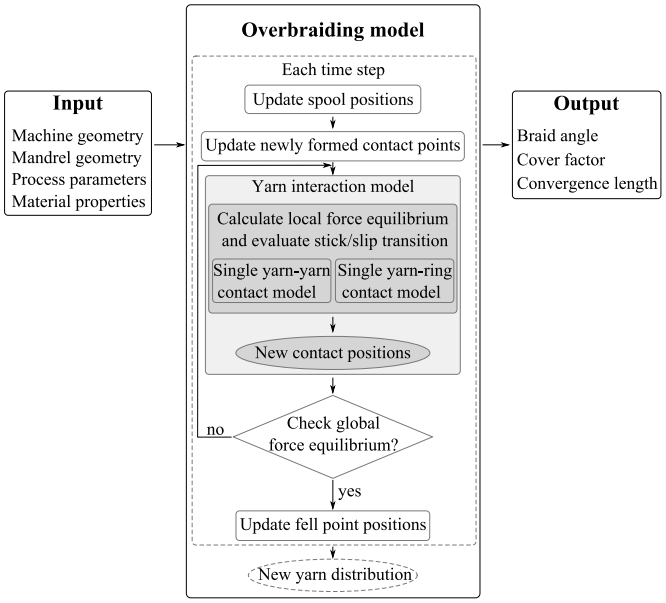

Fig. 2. Schematic illustration of the overbraiding model. Grey blocks highlight the main implementations of the new triaxial overbraiding model.

The study in Ref. [21] shows that the impact of yarn–yarn friction becomes more pronounced with an increased distance between the mandrel surface and the guide ring, which induces a larger convergence zone length. This study indicates that longer convergence zones and higher yarn tension lead to larger variations in the braid angle. This emphasizes the significance of including yarn interaction in overbraiding simulations to predict the resulting fiber distribution and prevent potential yarn damage [22,23]. Current overbraiding simulations assume a constant yarn–yarn coefficient of friction, as observed in prior studies [9,18,24], due to limited experimental data and the absence of more accurate constitutive models.

This study presents a new triaxial overbraiding model that accounts for yarn interactions and is suited for complex mandrel geometries. To achieve this, we propose extending the yarn interaction model previously introduced for the biaxial architecture [12] to the triaxial architecture. Various friction laws can be applied to the contact between yarns, allowing for a wide range of modeling options. To validate the model, we conducted triaxial overbraiding experiments using non-contact measurement methods for the braid angle and convergence zone length as a function of different UD tensions and initial mandrel positions. The experimental data was compared with the model predictions to assess the model's accuracy.

2. Triaxial overbraiding models

The overbraiding model, as schematically illustrated in Fig. 2, takes various inputs, including the machine geometry, mandrel geometry, process parameters, and material properties (e.g. the friction parameters between yarns). The model performs three tasks at every time step. First, a contact detector is used to identify newly formed contact points between the yarns, starting from the known positions of the spools. Second, the model solves the multiple contact points problem. This involves calculating the force equilibrium and slip at each yarn–yarn and yarn–ring contact point, then updating the contact coordinates. The contact points formed at the supply point are far from the center of the mandrel, and therefore, they have a very high sliding velocity (with loose contacts) until they pass the guide ring, resulting in fewer contact points in this region compared to number of contact point between the ring and the mandrel surface. Our previous paper [12] showed that the braid angle differed by only 1% when excluding the friction in the row of yarn–ring contacts. This indicates that a few numbers of contact rows from the supply point to the guide ring have a minor effect on the braid angle and can be neglected to reduce the complexity of the model.

At the end of this step, the global force equilibrium is checked. If the global force equilibrium is insufficient, the solving process is repeated by resolving the multiple contact points problem using the updated contact positions and forces from the previous iteration. It is noted that the algorithm no longer searches for the newly formed contact points in this resolving process. After satisfying the global force equilibrium, the contacts between yarns and mandrel are determined to relocate the fell points. The distribution of yarns is obtained at the end of each time step and serves as the initial configuration for the next time step. The output upon completion of the simulation includes the braid angle, cover factor, and convergence zone length at each location and time step.

Previous study developed and implemented the kinematic model [7] in BraidSim [25]. This kinematic model excludes the block of yarn interactions in Fig. 2, which led to inaccurate estimations of the braid angle. To improve its accuracy, several attempts have been made to incorporate yarn interaction models, as reported in Ref. [9,12]. In our previous study [12], we enhanced the yarn–yarn and yarn–ring contact model and used a frontal approach that effectively addresses the modeling of multiple contact points. This improvement enables the application of the model to complex mandrel shapes. However, the models were limited to biaxial overbraiding processes.

In this study, we present an extended yarn interaction model for triaxial overbraiding. This new model introduces a unidirectional yarn group, resulting in a more complex interaction system that has three times more contact points compared to biaxial overbraiding. We introduce an anisotropic force-dependent friction model for the single yarn–yarn contact, while the yarn–ring contact follows the same procedure as presented in [12]. The models for these contacts are illustrated in Fig. 3. The subsequent sections provide detailed information on the boundary conditions and solution procedures for each model.

2.1. Model assumptions

The triaxial overbraiding model is based on the following assumptions. Force equilibrium is evaluated on the yarn level, neglecting the effects of fiber entanglement [26] and yarn degradation [23] that occur during the process. The yarns are considered to be inextensible with zero resistance to bending, shearing and torsion. They are assumed to be constantly under tension and aligned with the force direction. Yarn-guide ring interactions are approximated as a point contact problem on a rigid circular contour, separately considering the forces in the yarn directions (using the capstan equation) and those transverse to the yarns, as further detailed in [12]. The mandrel surface is rigid and induces the yarns to stick completely to the mandrel surface upon contact. Static equilibrium is considered to be a suitable condition, ignoring any inertia terms.

2.2. Single contact models

2.2.1. Yarn–yarn contact model

Fig. 3a depicts a yarn–yarn contact model, in which two yarns make contact at point $\mathbf{C}_y$. The warp and weft yarns are identified as X and O, respectively. The yarns are fixed on one end at $\mathbf{A}_X$ and $\mathbf{A}_O$, while external forces $\mathbf{F}_X^{\text{ext}}$ and $\mathbf{F}_O^{\text{ext}}$ are applied on the opposite ends. These boundary conditions are initialized from the previous time step of the simulation. The objective is to determine the location of point $\mathbf{C}_y$ when the boundary conditions change. A more detailed description of the model can be found in [12].

At the start of the increment, an initial yarn coordinate system is established as $\mathbf{e}_1 \perp \mathbf{e}_2 \perp \mathbf{e}_3$, with the origin at $\mathbf{A}_X$. The basis vector $\mathbf{e}_1$ passes through the fixed points $\mathbf{A}_X$ and $\mathbf{A}_O$. Meanwhile, $\mathbf{e}_3$ resides

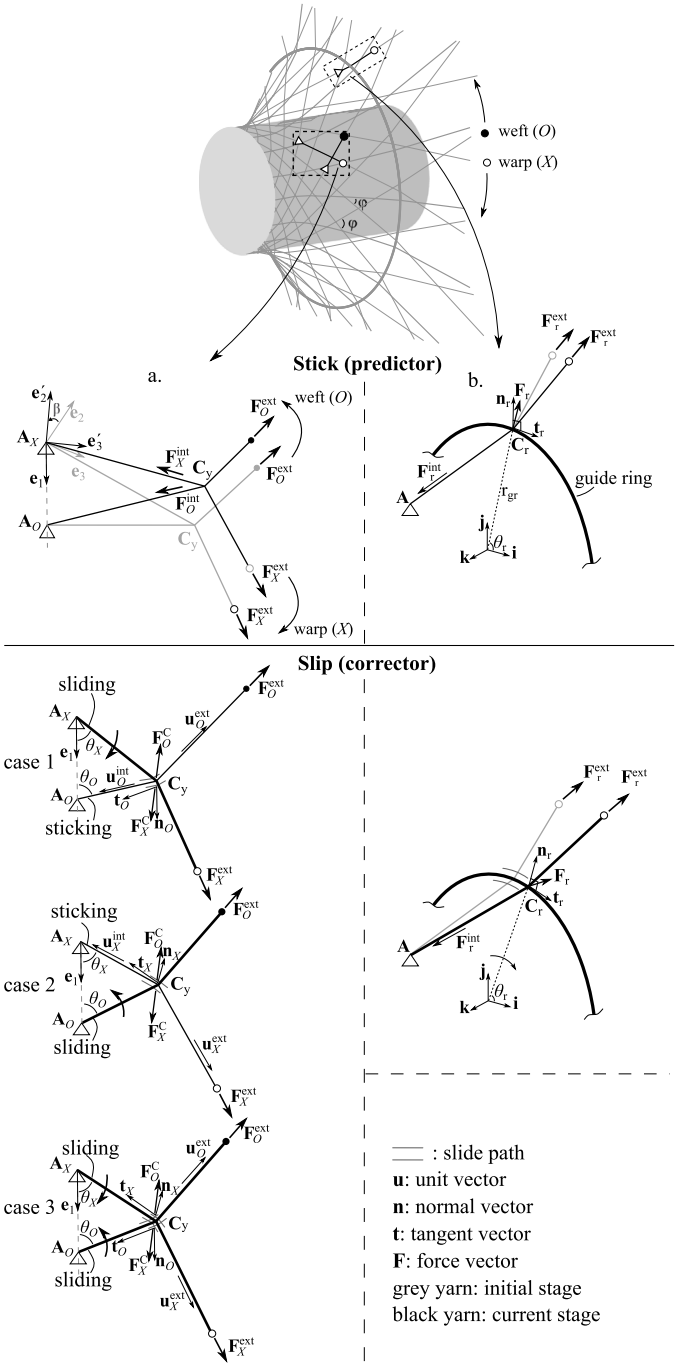

Fig. 3. Single contact point models with color-coded yarn representation: grey for the initial stage, black for the current stage. (a) Yarn–yarn contact model: the yarns at initial stage rotate to the yarns at equilibrium state via rotational angle β. The evaluation of the slipping function at equilibrium state reveals three slip cases. (b) Ring–yarn contact model: the yarn at the stick phase starts to slip as it reaches the slipping condition. The variation in θ_r indicates the direction of slip of the yarn over the guide ring. The boundary conditions remain unchanged throughout and after the solution step. The angle φ between the yarns is defined as inter-yarn angle.

within the plane formed by the yarn segments $\mathbf{C}_y\mathbf{A}_X$ and $\mathbf{C}_y\mathbf{A}_O$. With a gradual change in the external forces, the two yarns initially stick together without any relative movement. The reaction forces at the contact point $\mathbf{C}_y$ must be in equilibrium, given by:

$$\mathbf{F}_X^C + \mathbf{F}_O^C = \mathbf{0} \quad \text{with} \quad \mathbf{F}_X^C = \mathbf{F}_X^{int} + \mathbf{F}_X^{ext}, \quad \mathbf{F}_O^C = \mathbf{F}_O^{int} + \mathbf{F}_O^{ext}. \tag{2}$$

Here, $\mathbf{F}_X^C$ and $\mathbf{F}_O^C$ represent the reaction forces at the contact point, whereas $\mathbf{F}_X^{int}$ and $\mathbf{F}_O^{int}$ are the internal forces of the corresponding yarn. The equilibrium equation in (2) implies that the sum of the external forces is equal to the sum of the internal forces, but in the opposite direction. This can be expressed as:

$$\mathbf{F}_X^{int} + \mathbf{F}_O^{int} = -(\mathbf{F}_X^{ext} + \mathbf{F}_O^{ext}). \tag{3}$$

Since the yarn segments $\mathbf{C}_y\mathbf{A}_X$ and $\mathbf{C}_y\mathbf{A}_O$ align with $\mathbf{F}_X^{int}$ and $\mathbf{F}_O^{int}$, respectively, the relation in Eq. (3) indicates that these segments must rotate around $\mathbf{e}_1$ at an angle, for example via β to a new plane that includes both ($\mathbf{F}_X^{ext} + \mathbf{F}_O^{ext}$) and $\mathbf{e}_1$. This leads to a new local yarn coordinate system $\mathbf{e}_1 \perp \mathbf{e}_2' \perp \mathbf{e}_3'$ where the slip phase is solved.

To account for slip, the Eulerian on Lagrangian method is employed [12]. This method involves introducing two Lagrangian degrees of freedom, represented by the rotational angles θ_O and θ_X, which allow for the weft yarn to slip over the warp yarn and vice versa. The degrees of freedom in each direction are determined by slip functions, given by:

$$\Psi_y(\theta_O) = \left\|\mathbf{F}_O^t\right\| - f_y, \quad \Psi_y(\theta_X) = \left\|\mathbf{F}_X^t\right\| - f_y, \tag{4}$$

where $\mathbf{F}^t$ is the tangential force at the contact point, which can be calculated as:

$$\mathbf{F}_{O,X}^t = \mathbf{F}_{O,X}^C \times \mathbf{n}_{O,X} \quad \text{with} \quad \mathbf{n}_{O,X} = -\frac{\mathbf{u}_{O,X}^{int} + \mathbf{u}_{O,X}^{ext}}{\left\|\mathbf{u}_{O,X}^{int} + \mathbf{u}_{O,X}^{ext}\right\|}, \tag{5}$$

and f_y is the maximum frictional force. If the tangential force is less than the maximum frictional force, or $\Psi_y < 0$, the yarns stick. However, if the tangential force reaches the maximum frictional force, or $\Psi_y \geq 0$, the yarns slip.

The slip analysis results in three possible scenarios. Case 1: the warp yarn moves $\Psi_y(\theta_X) \geq 0$ while the weft yarn remains stationary $\Psi_y(\theta_O) < 0$ indicating θ_O is unchanged. Case 2: the weft yarn moves $\Psi_y(\theta_O) \geq 0$ while the warp yarn remains stationary $\Psi_y(\theta_X) < 0$ indicating θ_X is unchanged. Case 3: both yarns move $\Psi_y(\theta_{X,O}) \geq 0$. These slip cases are illustrated in Fig. 3a. In the event of slip, a solution for the Lagrangian variables θ_O and θ_X is required. This can be obtained by solving $\Psi_y(\theta_{X,O}) = 0$. The updated contact coordinate $\mathbf{C}_y$ is found using the equation:

$$\mathbf{C}_y = \mathbf{A}_X + p \cdot \mathbf{u}_X^{int} \quad \text{where} \quad \mathbf{u}_X^{int} = \frac{\mathbf{F}_X^{int}}{\left\|\mathbf{F}_X^{int}\right\|} \tag{6}$$

where $\mathbf{u}_X^{int}$ is the unit vector of the yarn segment $\mathbf{C}_y\mathbf{A}_X$. The parameter p represents the Eulerian degree of freedom, allowing the material to pass through the contact point and leading to a new length of the yarn segment. This parameter can be determined by solving the intersection of the two yarns problem using the known values of θ_O and θ_X. A more detailed description of the single yarn–yarn model can be found in Ref. [12].

2.2.2. Friction laws

The friction function f_y describes the frictional behavior between yarns by using different friction models. In this study, we employed and evaluated two friction models: isotropic Amontons' friction and anisotropic Howell friction. In the following sections, we discuss these friction models in more detail.

Isotropic Amontons' friction. The isotropic friction model, based on Amontons' friction law [27,28], provides a simplified representation of friction. It assumes that the maximum frictional force is independent of the loading rate and the inter-yarn angle [27,28]. The mathematical formulation of this friction law can be described as:

$$f_{y_{O,X}} = \mu_{iso} \left\|\mathbf{F}_{O,X}^n\right\| \quad \text{where} \quad \mathbf{F}_{O,X}^n = (\mathbf{F}_{O,X}^C \cdot \mathbf{n}_{X,O})\mathbf{n}_{X,O}, \tag{7}$$

where the maximum frictional force f_y is proportional to the coefficient of friction (CoF) μ_{iso} and the normal force $\mathbf{F}^n$.

Anisotropic Howell friction. The actual friction between yarns is more complicated in practice and depends on the normal force and the angle between the yarns, as experimentally observed in Refs. [29–32]. In a previous study (see Ref. [33]), we proposed an anisotropic friction law based on the experimental findings. The friction law is an extension of the well-known Howell friction as described in [34,35]. This study incorporates the anisotropic Howell friction using the following equation:

$$f_{y_{O,X}} = k(\varphi)\left\|\mathbf{F}^{n}_{O,X}\right\|^{n(\varphi)} \quad \text{and} \quad \mu_{aniso_{O,X}} = k(\varphi)\left\|\mathbf{F}^{n}_{O,X}\right\|^{n(\varphi)-1}. \tag{8}$$

The parameter φ is the angle between yarns as illustrated in Fig. 3. The functions k(φ) and n(φ) express the dependencies of the friction on the inter-yarn angle and are described by two power law functions:

$$k(\varphi) = \frac{k_{90}}{(\sin\varphi)^{n_k}} \quad \text{and} \quad n(\varphi) = (\sin\varphi)^{n_n}. \tag{9}$$

These equations involve three material-dependent constants k_{90}, n_k, and n_n. These constants can be obtained from the experimental data of yarn–yarn friction, which is available in the repository reported in Ref. [36]. This repository also contains the details of the experimental method and procedure used to measure the friction and to determine the model parameters.

2.2.3. Yarn–ring contact model

The yarn–ring contact model was used as presented in Ref. [12]. In Fig. 3b, a yarn is in contact with a ring at point $\mathbf{C}_r$. The yarns' ends have a prescribed position at point **A** and an applied external force $\mathbf{F}^{ext}_r$, while the output of the model is the position of contact point $\mathbf{C}_r$ as the boundary conditions change. The model includes a Lagrangian degree of freedom θ_r to describe position changes in the ring coordinate system (**i**, **j**, **k**):

$$\mathbf{C}_r = r_r \begin{bmatrix} \cos\theta_r \\ \sin\theta_r \\ 0 \end{bmatrix}, \tag{10}$$

with r_r the guide ring radius. Yarn and guide ring undergo slip via a stick–slip mechanism in both longitudinal and transverse directions as described in Ref. [12]. The slip function used to evaluate the stick–slip process is expressed as:

$$\Psi_r(\theta_r) = \left\|\mathbf{F}^{t}_r\right\| - f_r. \tag{11}$$

Here, $\mathbf{F}^{t}_r$ is the tangential force and $f_r = \mu_r \left\|\mathbf{F}^{n}_r\right\|$ is the maximum friction force, which is defined using Amontons' friction with the coefficient of friction μ_r determined experimentally. A value of $\mu_r = 0.17$ is used, as reported in the study by Cornelissen et al. [29], for the contact between carbon yarn and steel with a root mean square roughness of 1.1 ± 0.4 μm.

2.2.4. Implementation of the single contact models

This section presents the implementation of the single contact models. When the slip occurs or $\Psi_{y/r} \geq 0$, the solutions of the Lagrangian variables are needed. These can be obtained by solving the slip functions:

$$\Psi_y(\theta_O, \theta_X) = 0, \quad \Psi_r(\theta_r) = 0. \tag{12}$$

The functions exhibit a high level of non-linearity, even more when accounting for anisotropic friction between yarns. Therefore, an iterative procedure based on the Newton–Raphson scheme was employed to obtain the solution of the Lagrangian variables $\theta_{O,X}$ and θ_r. Details of this scheme can be found in Fig. 4.

The algorithm includes two main steps: a predictor step and a corrector step as also illustrated in Fig. 3. In the predictor step, Eq. (4) or Eq. (11) is computed to determine whether the yarns are in the sliding stage; if so, then the corrector step is executed. The objective of this step is to find the correct values of the Lagrangian variables $\theta_{O,X}$ and θ_r that satisfy Eq. (12). The Newton–Raphson scheme starts

(1) Predictor	check if $\Psi\left(\theta_{O,X,U/r}\right) > 0$? yes → slip, go to (2), else → stick ($\theta_{O,X,U/r}$ unchanged)
(2) Corrector	Newton Raphson iteration for solving $\Psi\left(\theta_{O,X,U/r}\right) = 0$
(2.1) Objective	$\Psi = \left\|\mathbf{F}^{t}\left(\theta_{O,X,U/r}\right)\right\| - f_{y/r} = 0$
(2.2) Linearization	$\Psi \approx \Psi\|_{(\theta_{O,X,U/r})_k} + \underbrace{\frac{\partial\Psi}{\partial\left(\theta_{O,X,U/r}\right)_k}}_{\mathbf{J}_k} .\Delta(\theta_{O,X,U/r})_k = 0$
(2.3) Solve $\Delta(\theta_{O,X,U/r})_k$	$\Delta(\theta_{O,X,U/r})_k = -[\mathbf{J}_k]^{-1}.\Psi$
(2.4) Update	$(\theta_{O,X,U/r})_{k+1} = (\theta_{O,X,U/r})_k + \Delta(\theta_{O,X,U/r})_k$,
(2.5) Repeat (2.1) → (2.4)	stop if $\Psi\left(\theta_{O,X,U/r}\right)_k < \varepsilon$

Fig. 4. Newton–Raphson scheme for solving non-linear slip function.

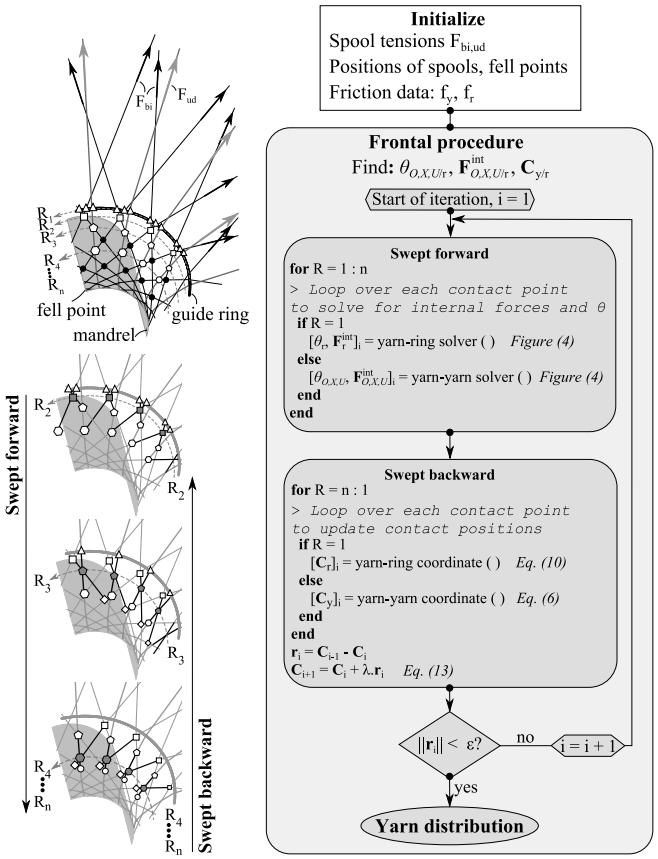

Fig. 5. Illustration of the multiple contact point model with the row discretization and iterative frontal procedure for each time step. Rows of black dots on the top figure indicate no contacts between the biaxial yarns.

with the calculation of the residual function at step (2.1). Next, a linearization function is determined at step (2.2) where the Jacobian matrix is approximated using a backward finite difference method. The variables $\Delta(\theta_{O,X,U/r})_k$ are the solution increments after each iteration as calculated in step (2.3). The Lagrangian variables are updated at step (2.4). This iterative procedure continues until a predefined tolerance is met. It is noted that the Lagrangian variables $\theta_{O,X}$ and θ_r were mistakenly labeled as the Eulerian variables in the authors' earlier publication Ref. [12].

2.3. Multiple yarn interaction model

A fast frontal approach, previously utilized in Ref. [9,12], is applied in this study to address the multiple contact points problem. The aim of this method is to obtain the updated axial forces of the yarn segments

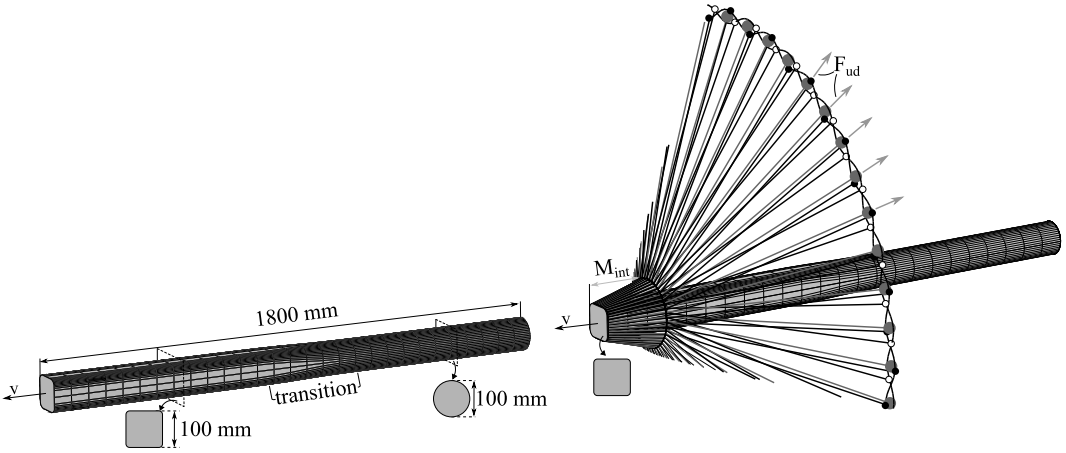

Fig. 6. Illustration of machine geometry: mandrel with square and circular cross-sections, including a transition cross-section positioned between 800 mm to 1000 mm. Process parameters are analyzed by varying the initial mandrel position (M_{int}) and the UD tension (F_{ud}).

$\mathbf{F}^{int}_{O,X,U/r}$ and the corresponding contact point coordinates $\mathbf{C}_{y/r}$, which fulfill the contact force equilibrium Eq. (2) and slip function Eq. ((4), (11)) at each contact point. This approach is extended to accommodate the regular pattern between the weft yarns, warp yarns, and UD yarns in triaxial overbraiding.

The boundary conditions of the model consist of the known positions of the spools, the tensions $F_{bi,\ ud}$ exerted by these spools, and the positions of the fell points from the previous time step. The boundary conditions remain unchanged throughout each time step. The frontal procedure in each time step is initiated by defining the rows of contact points within the convergence zone. The contact rows are distinguished using different symbols, depicted in Fig. 5. Starting from the guide ring, all contact points are grouped as R_1. The contacts between the weft and warp yarns on the left of the UD yarns are defined as R_2. The next row, R_3, includes the contact between weft yarn and UD yarn. This grouping is continued until the fell point at R_n is reached. It is important to note that due to the interlacing order, there is no contact between the weft and warp yarns on the right of the UD yarns (see Fig. 1 bottom), i.e. the row of black dots between the rows R_3 and R_4 as shown in Fig. 5. The frontal procedure is a two-loop algorithm that consists of a swept forward loop and a swept backward loop. The swept forward loop evaluates the single contact models at each contact point from R_1 to R_n to obtain the internal force vectors $\mathbf{F}^{int}_{O,X,U/r}$ and the corresponding angles $\theta_{O,X,U/r}$. The resultant internal forces are then used as the external forces for the next row. The swept backward loop reversely evaluates each contact point from R_n to R_1, to update the contact coordinates $\mathbf{C}_{y/r}$ (see Eq. (6), (10)).

In order to obtain a stable solution, multiple frontal procedures are required, and the minimum residual method is used to update the contact coordinate matrix at the end of each iteration [12]. The updated coordinate of the contact points is given by:

$$\mathbf{C}_{i+1} = \mathbf{C}_i + \lambda.\mathbf{r}_i, \tag{13}$$

where i is the iteration number of the frontal procedure loop and $\mathbf{r}_i = \mathbf{C}_{i-1} - \mathbf{C}_i$ is the difference in the contact coordinate matrix between the current and previous iteration. The damping factor λ can be optimized, as explained in Ref. [12]. The algorithm utilized in this study is depicted in Fig. 5 and has been implemented using MATLAB®.

3. Triaxial overbraiding experiments

Overbraiding experiments were performed to measure the convergence zone length and braid angle with minimum interference in the process. The experimental data serves to validate the proposed triaxial overbraiding model.

3.1. Yarn material and mandrel

The experimental tests were carried out using two types of carbon yarns, namely Torayca T300J.6K.PU for the biaxial yarns and Hextow IM7.12k.GP for the UD yarns, in untwisted conditions. The mandrel had a mixed cross-sectional geometry, consisting of a rounded square cross-section and a circular cross-section, with a transition zone in the middle. The geometry of the mandrel is illustrated in Fig. 6.

3.2. Measurement method of convergence zone length

An experimental setup was developed to measure the convergence zone length during triaxial overbraiding (see Fig. 7). A NIKON D5600 camera was used, offering a resolution of 2992×2000 pixels and 30 frames per second. The camera was positioned perpendicular to the region of interest (ROI), where the convergence zone length was visible. A reference length was mounted parallel to the ROI to ensure accurate mapping of the pixel coordinates to the actual longitudinal coordinate. A white background was used to enhance the black surface contours of the braid. As illustrated in Fig. 7, the experimental procedure involved recording a video of the triaxial overbraiding process, followed by converting each frame to black and white to facilitate boundary recognition of the braided shape. A fifth order polynomial function was fitted smoothly to both sides of the braid. The point with a horizontal slope of $\partial y/\partial x = 0$ was defined as the fell point. The convergence zone length was then calculated as the distance between the guide ring and the fell point. This procedure was repeated for each frame.

3.3. Measurement method of braid angle

Image analysis was used to measure the braid angle, as documented in Ref. [37,38]. The measurement procedure, illustrated in Fig. 8, involves capturing an image of the braid after manufacturing. The

Table 1
Machine configuration of the overbraiding processes.

Parameter	Value
Spool plane radius, r_s [mm]	850
Guide ring radius, r_r [mm]	102.5
Spool number of weft, warp, UD group	48
Spool pattern	Regular
Take-up speed, v [mm/s]	15.7
Angular spool velocity, ω [°/s]	18
Target braid angle using Eq. (1) [°]:	
Square cross section	50
Circular cross section	45

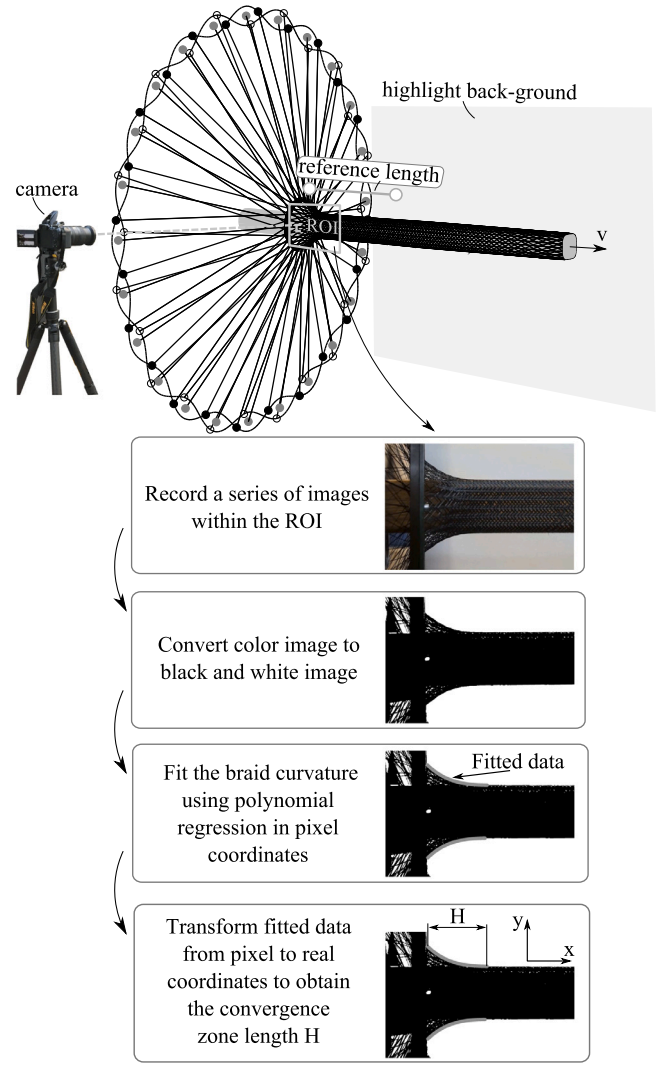

Fig. 7. Schematic illustration of experimental setups to measure the convergence zone length.

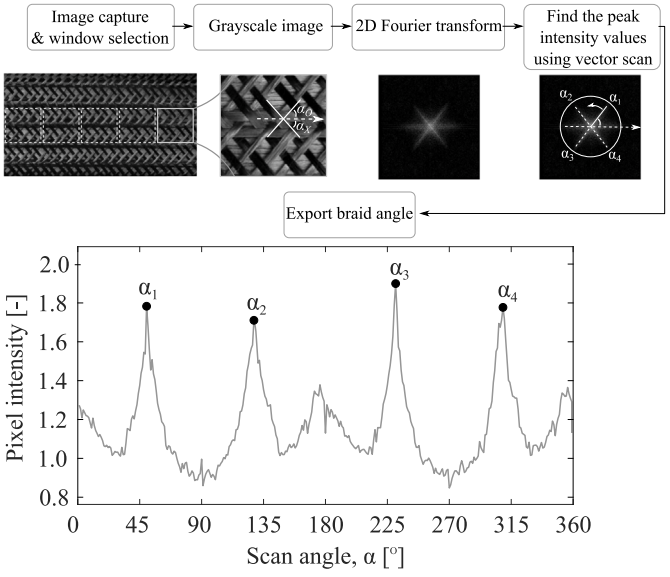

Fig. 8. Flowchart of experimental measurement of braid angle using image analysis method.

image was converted to greyscale and divided into square segments. In each square segment, a two-dimensional discrete Fourier transform was computed using the `fft2` function in MATLAB®, with the resulting spectrum center-shifted using the `fftshift` function. A rotated vector search was subsequently performed to find the peak intensities in the spectrum, and the four resulting peaks were designated as $\alpha_1, \alpha_2, \alpha_3$, and α_4, as shown in Fig. 8 (bottom). The mean of α_1 and $\alpha_3 - 180°$ corresponds to the weft braid angle α_O, while the mean of $180° - \alpha_2$ and $360° - \alpha_4$ corresponds to the warp braid angle α_X. This process of image analysis was conducted at the central region around the circumference and along the length of the mandrel.

3.4. Experiment

The triaxial overbraiding tests were conducted at EuroCarbon B.V. in the Netherlands on a 96 spool carriers overbraiding machine equipped with a circular guide ring. The dimensions of the machine are provided in Table 1.

Six experiments were conducted to examine the influence of the UD yarn tension and the initial mandrel position (see Fig. 6) on the braid angle and the convergence zone length. In addition, one experiment was performed without the UD yarns. Table 2 presents the test matrix, which incorporates various machine parameters. The square cross section of the mandrel was the starting point of the overbraiding process. It is noted that the initial distance from the tip of the square cross section of the mandrel to the guide ring plane is the initial mandrel position M_{int}. This quantity is different from the braided length L which is the distance from the starting tip of the mandrel to the fell point.

The influence of the UD yarn tension on the braiding process was investigated in tests 1, 2, and 3, where the UD yarn tension was set at nominal values of 1 N, 3 N and 6 N, while maintaining a constant biaxial yarn tension of 1.85 ± 0.65 N. The tension of the UD yarns in each spool was controlled using a spring system, ensuring a constant tension throughout the experiment [6]. The axial force of all UD yarns was manually measured prior to and during the experiment using a tension meter with three rollers. The tension force of the yarn is measured by guiding the yarn through the rollers, resulting in deflection of the middle roller, which presses against a load cell. To ensure accuracy, the tension meter was calibrated using a known weight suspended from the yarn. Prior to the experiment, the applied tension on the UD yarns was verified by aligning the rollers of the tension meter perpendicularly to the yarns. The tension of the yarns was periodically verified during the process to ensure it remained at the correct level, with a maximum deviation of approximately ±0.2 N.

The effect of the initial mandrel position M_{int} was studied in tests 2, 4, and 5, using values of M_{int} at 150 mm, 0 mm, and 300 mm while the other parameters were held constant. In the experiments, the yarns' ends were attached to the tip of the mandrel together using adhesive tapes. The mandrel was then moved in to pull the yarn to the desired initial position. The distance between the mandrel tip and the guide ring was checked manually before starting the machine.

Lastly, the effect of the absence of UD yarns was examined and compared to the lowest UD tension of 1 N. Table 1 shows the other process parameters and the target braid angles which are calculated using Eq. (1) for each cross section. The braid angle and convergence zone length were measured using the previously described methods.

3.5. Experimental results

Effect of UD tension. Fig. 9a depicts the evolution of the braid angle and convergence zone length with respect to the braided length, for varying UD tensions. The data reveals four distinct states: an unsteady state, a steady state at the square cross-section, a transition, and a second steady state at the circular cross-section. Increasing the UD tension results in a higher initial braid angle, while the steady state is reached at approximately 500 mm of braided length, independent of

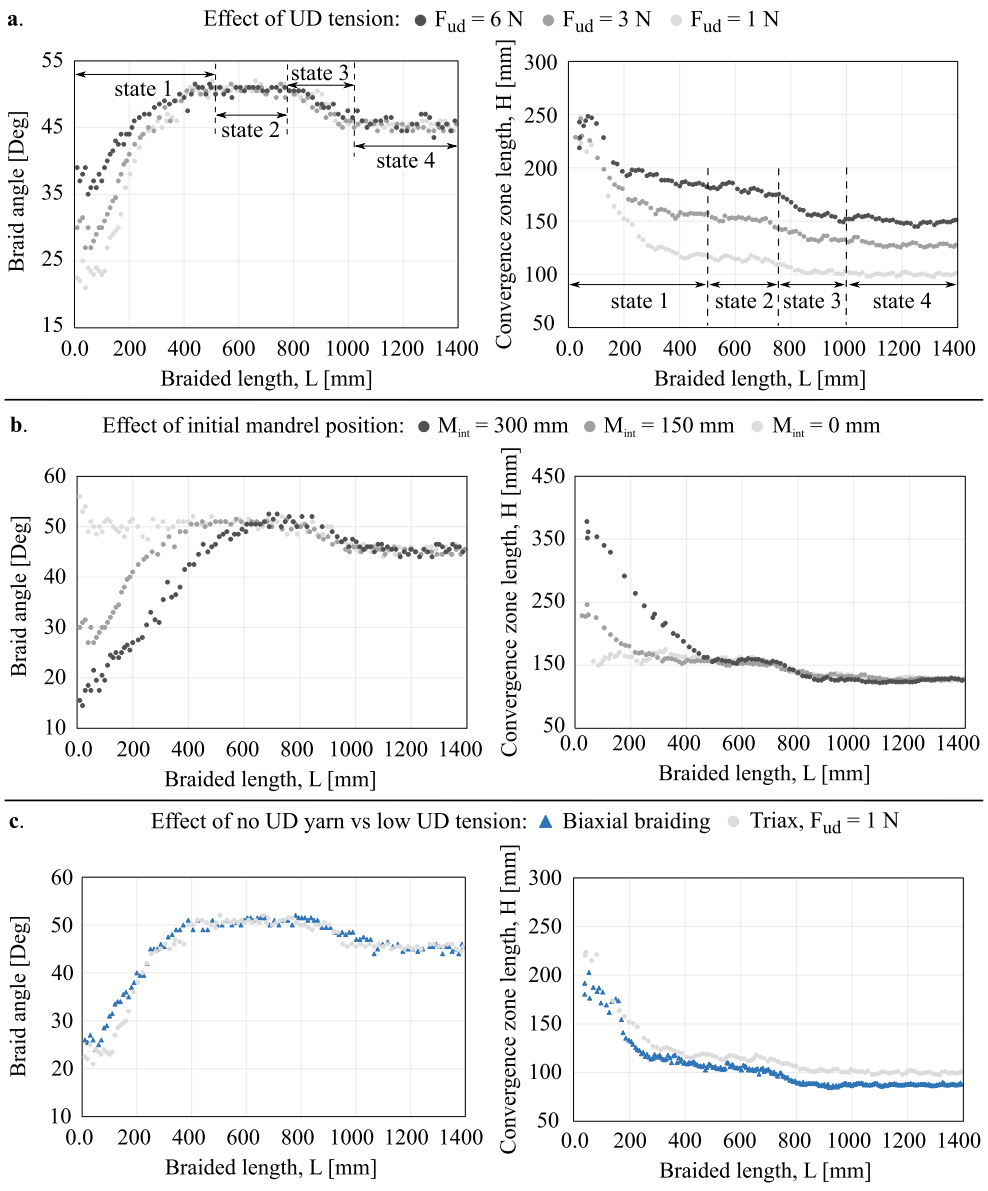

Fig. 9. Experimental results demonstrate the effects of process parameters shown in Table 2 on braid angle and convergence zone length. (a) Effect of UD tension (test no. 1, 2, 3). (b) effect of initial mandrel position (test no. 2, 4, 5). (c) Effect of triaxial overbraiding with low UD tension versus biaxial overbraiding (test no. 1, 6). The data reveals four distinct states: state 1 – unsteady state; state 2 – steady state at the square cross-section; state 3 – transition; and state 4 – steady state at the circular cross-section.

UD tension, where all braid angles reach the same constant value. The convergence zone length shows a similar trend with respect to braided length, and converges to distinct constant values in the steady state. Higher UD tension results in a more open braid within the convergence zone. This UD tension allows the yarn to slide further before contacting the mandrel surface. This results in a higher convergence zone length compared to the case of a lower UD tension, for which the convergence zone length is shorter.

Effect of initial mandrel position. Fig. 9b presents the effect of the initial mandrel position on the braid angle and corresponding convergence zone length. An increase in the initial mandrel position results in a decrease in the initial braid angle. The braid angle reaches steady state almost instantly for M_{int} = 0 mm, exhibiting a faster convergence compared to M_{int} = 150 mm and M_{int} = 300 mm. These processes reach the steady state at a braided length of 400 mm and 550 mm, respectively. Although the convergence zone length starts at different initial values for different values of M_{int}, it eventually converges to the same value at the steady state.

Effect of reinforcement structure. Fig. 9c compares triaxial overbraiding with a low UD tension (F_{ud} = 1 N) with biaxial overbraiding (absence of UD yarn) in terms of the convergence zone length and braid angle. Both sets of data exhibit a similar trend, with an average difference of only 5° in braid angle during the unsteady state. Furthermore, biaxial overbraiding results in a convergence zone length that is slightly shorter (12 mm on average) compared to low UD tension.

4. Simulation results and discussion

Overbraiding simulations were performed using the same machine geometry and process parameters as in the experiments. The biaxial overbraiding process was simulated using the model developed in [12]. The computational cost of the triaxial and biaxial overbraiding simulation is summarized in Table 3. This table shows the relationship between the number of contact rows, with the corresponding number of contact points progressively developing throughout the simulation, the computational time for each step and the total execution time. The findings demonstrate a nearly linear correlation between the number

Table 2
Test matrix of the overbraiding experiments and simulations.

No.	Architecture	UD tension, F_{ud} [N]	Biaxial tension, F_{bi} [N]	M_{int}[mm]
1	Triaxial braid	1	1.85	150
2	Triaxial braid	3	1.85	150
3	Triaxial braid	6	1.85	150
4	Triaxial braid	3	1.85	0
5	Triaxial braid	3	1.85	300
6	Biaxial braid	–	1.85	150

of contact points and the computational cost. Despite the current implementation in MATLAB®, the results demonstrate reasonable computational efficiency, with time steps being completed within seconds and the total computational time in the order of minutes on a laptop with an Intel(R) i7-8750H CPU at 2.2 GHz processor and 16 GB of RAM . It is noted that the computation time is independent of the type of friction, as the current implementation solves the sliding problem Eq. (12) in all these cases.

4.1. Numerical study 1: isotropic Amontons' friction

In order to evaluate the effect of a uniform isotropic friction coefficient on the predicted braid angle distribution under different UD tensions, simulations were conducted assuming Amonton's friction with CoFs of 0.0, 0.25, to 0.5 and UD tensions of 1 N, 3 N and 6 N.

Fig. 10 shows the simulation results when using the isotropic Amontons' friction compared to the experimental data. The simulations predict the same four distinct stages as in the experiment. Once the process reaches the steady state, both simulated and experimental data show the same values of braid angle. Increasing the coefficient of friction results in a lower initial braid angle. At the same friction coefficient, increasing the UD tension results in a higher start-up braid angle during unsteady state, similar to what was observed during the experiment. However, the initial braid angle exhibits only a slight variation of 4° when utilizing the maximum and minimum UD tensions of 1 N and 6 N. For instance, when the friction coefficient μ_{iso} equals 0.25, the initial braid angle ranges from 25° to 29°. In contrast, experimental observations reveal a significant difference in the initial braid angle, with variations of up to 14°, from 18° to 32°. The difference in the initial braid angle between the experiment and the simulation when varying the UD tension is attributed to the use of a constant CoF in each analysis. However, it is worth noting that the CoF between the yarns is influenced not only by the normal force which varies due to the UD tension, but also by the inter-yarn angle, as evident in the friction data shown in Fig. 11.

Table 4 presents a comparative analysis of the maximum braid angle deviations between simulation and experimental results for different applied UD tensions. In this analysis, the difference in braid angle between the simulated and experimental data was calculated across all states. Subsequently, the maximum deviation in braid angle was identified. The corresponding equation was provided in Table 4. The results indicate that, at the lowest UD tension of 1 N, the measured braid angle exhibited a better agreement with a higher friction coefficient of 0.5, yielding a deviation of 1.1°. However, when utilizing the same friction

Table 3
Computational time analysis for the triaxial and biaxial overbraiding simulation.

Contact points	Contact rows	Yarns/group	Computational cost [s/step]	
			Triax. overbraiding	Biax. overbraiding
480	10	48	1.56	0.97
960	20	48	3.41	2.11
1440	30	48	6.34	4.03
			∑43.7 mins	∑27.3 mins

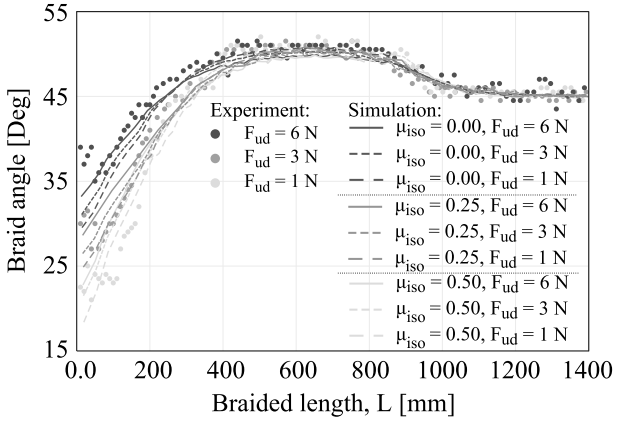

Fig. 10. Comparison of experimental data and simulation data using the isotropic friction model. The constant coefficient of friction μ_{iso} varies with three different values of 0.0, 0.25, and 0.5. The UD tension was varied for each value of μ_{iso}.

coefficient value of 0.5, a higher discrepancy was observed between the simulated and experimental data for UD tensions of 3 N and 6 N, with deviations of 5.4° and 12.3°, respectively. With the UD tension of 3 N, the best agreement was achieved with a friction coefficient of 0.25, resulting in a deviation of 1.4°. Conversely, for the UD tensions of 1 N and 6 N, larger differences of 3.9° and 6.4° were observed.

The measured braid angle at a UD tension of 6 N closely matched the simulation results with a friction coefficient of 0.0, exhibiting a small deviation of only 1.5°. However, substantial deviations of 7.6° and 4.2° were observed for the UD tensions of 1 N and 3 N, respectively, when a friction coefficient of 0.0 was used.

The findings demonstrate that the braid angle during the unsteady state is primarily influenced by the CoF, while the effect of the UD tension is relatively small. Moreover, the results suggest that describing yarn–yarn friction using an isotropic Amontons' friction is insufficient to accurately predict the braid angles for different UD tensions.

4.2. Numerical study 2: anisotropic Howell friction

In the second study, the anisotropic Howell model was used for the yarn–yarn friction, which depends on the inter-yarn angle and normal force at the contact point. The material parameters for the friction model Eq. (8)–(9) were fitted to the experimental data as reported in the repository referenced in [36] for the contacts between T300J on T300J and T300J on IM7. Fig. 11 shows the measured friction data as a function of the normal force and the inter-yarn angle for the two contact pairs in dry condition. The anisotropic friction model given in Eq. (8) was fitted to the experimental data using a single set of the three parameters for each contact pair. The parameters of the anisotropic

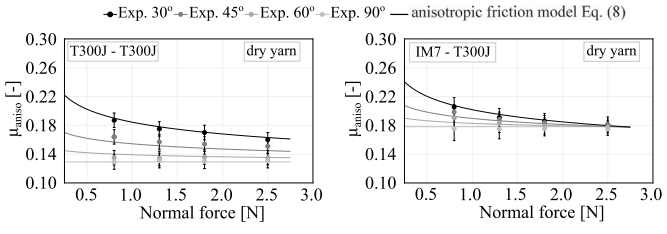

Fig. 11. Yarn–yarn friction data for the two pairs of contact used in the overbraiding experiments: T300J on T300J and T300J on IM7, reported in [33,36]. The dots show the friction coefficient measured in dry condition as a function of the normal force and the inter-yarn angle. The lines show the fitted data from the anisotropic friction model given by Eq. (8), using a single set of parameters for both contact pairs, as listed in Table 5.

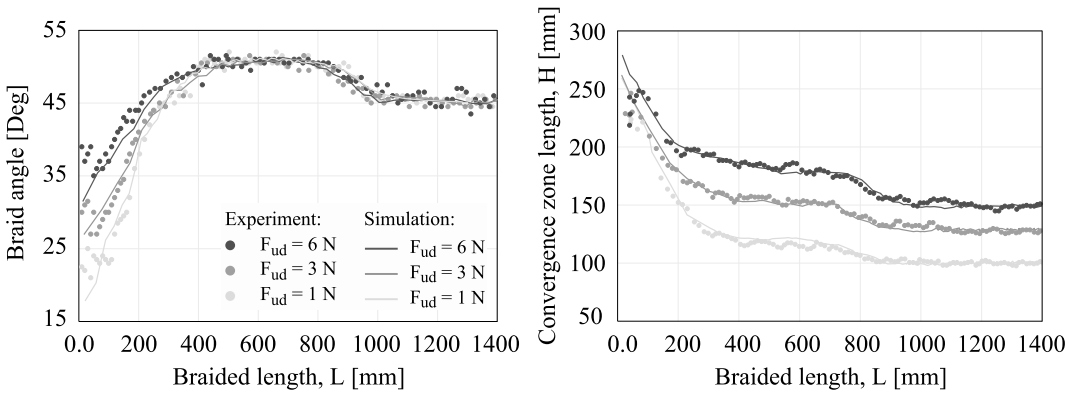

Fig. 12. Comparison of experimental and simulation data in triaxial overbraiding. The simulations utilized the anisotropic Howell friction law for the contacts between yarns.

Table 4
Comparison of maximum braid angle difference between simulation and experiment.

Sim. study	Friction model	$\Delta\alpha^{max}_{F_{ud}=i} = \max\lvert\alpha^{sim}_{F_{ud}=i} - \alpha^{exp}_{F_{ud}=i}\rvert$		
		$\Delta\alpha^{max}_{F_{ud}=1\ N}$ [°]	$\Delta\alpha^{max}_{F_{ud}=3\ N}$ [°]	$\Delta\alpha^{max}_{F_{ud}=6\ N}$ [°]
Study 1	$\mu_{iso} = 0.0$	7.6	4.2	1.5
	$\mu_{iso} = 0.25$	3.9	1.4	6.4
	$\mu_{iso} = 0.5$	1.7	5.4	12.2
Study 2	μ_{aniso}	1.4	1.6	1.7

Howell friction equation are presented in Table 5. Here, the value of k_{90} represents the CoF for orthogonal yarns, whereas the exponents n_k and n_n were found by linear least squares fitting Eq. (9) to the experimental data. Our measurements of the CoF and the fitting procedure of the anisotropic friction model were discussed in Ref. [33].

Fig. 12 and Table 4 compare the results of simulations using the anisotropic Howell friction law with the experimental data. The anisotropic Howell friction model significantly improves the accuracy of braid angle prediction compared to the previous numerical studies using isotropic Amontons' friction. The results of the simulated and experimental data showed a small maximum difference, with only 1.4°, 1.6°, and 1.7° for UD tensions of 1 N, 3 N, and 6 N, respectively. The simulated convergence zone length also agrees well with the experimental measurements.

These findings can be explained by the friction coefficient as obtained from the anisotropic Howell model, which is illustrated in Fig. 13. The anisotropic friction coefficient, represented as μ_{aniso}, is calculated as the ratio of the sliding friction force (Eq. (8)) to the normal force. The CoFs using the three UD tensions are consistently plotted at the unsteady state (t_1), in the steady state at the square cross-section (t_2), and in the steady state at the circular cross-section (t_3). The CoFs increase as the UD tension decreases, particularly at the contacts between the UD and biaxial yarns. This behavior is consistent with the force-dependence of the anisotropic Howell friction law. The CoFs are very high ($\mu_{aniso} \approx 1.0$) near the guide ring, where the inter-yarn angles and normal forces are small, and decrease ($\mu_{aniso} \approx 0.2$) as the yarns approach the fell point. The higher CoFs at low UD tension prevent yarn slip and promote earlier interaction with the mandrel, resulting in a shorter convergence zone length. In the steady state, the CoFs are smaller compared to the values in the unsteady state. This is because the new contact points are formed at larger inter-yarn angles, which results in a smaller CoF.

The triaxial overbraiding simulation using anisotropic friction was further validated with the experimental data of different initial mandrel positions. As shown in Fig. 14, the simulated data show good agreement with the experimental trend, with a maximum deviation of only 1.5° in braid angle and 31 mm in the convergence zone length. In a previous study [12], it was noted that the convergence zone length during steady state is sensitive to the CoF. The present study's results confirm this observation and indicate that the friction law used in the simulation accurately represents yarn–yarn contact during actual overbraiding. The starting position of the mandrel significantly affects the results, as observed in both experimental data and simulations. Furthermore, the initially random distribution of yarns around the mandrel's circumference can lead to variations in the braid angle at the beginning of the process. This can be observed in the experimental data shown in Fig. 9.

Fig. 15 presents the final validation study in which anisotropic friction was employed in triaxial overbraiding with low UD tension (F_{ud} = 1 N) and biaxial overbraiding simulations. The simulation results for both machine configurations agree well with the experimental data. The higher number of contact points in triaxial overbraiding leads to an increased friction between yarns, preventing slip and resulting in a lower start-up braid angle compared to biaxial overbraiding. The UD yarn group has a discernible impact on convergence zone length, yet the difference between triaxial overbraiding with low UD tension

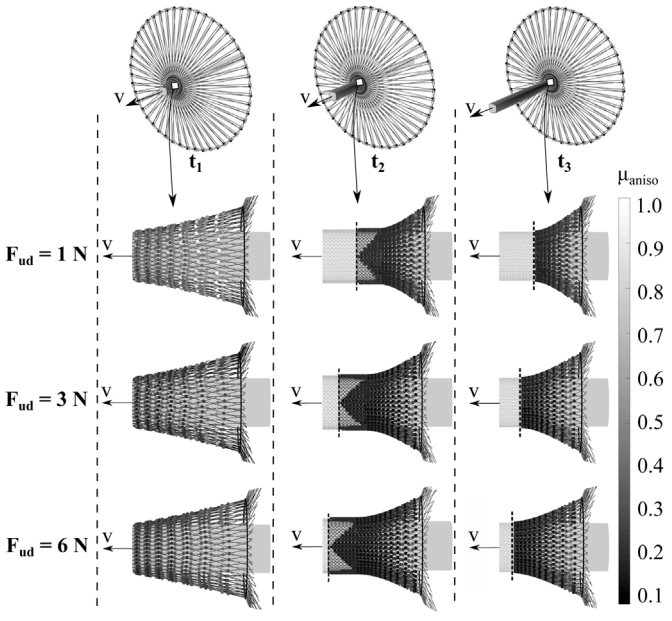

Fig. 13. Triaxial overbraiding simulations using anisotropic friction. The coefficients of friction calculated using the anisotropic Howell friction model are plotted as greyscale dots at each contact point with varying input values of UD tensions of 1 N, 3 N, 6 N, and at various stages of the braiding process: at the beginning (t_1), during the steady state at the square cross-section (t_2), and during the steady state at the circular cross-section (t_3). The coefficients of friction data are graphed from the fell points to the guide ring, with the dashed line indicating the farthest fell point from the guide ring at each stage.

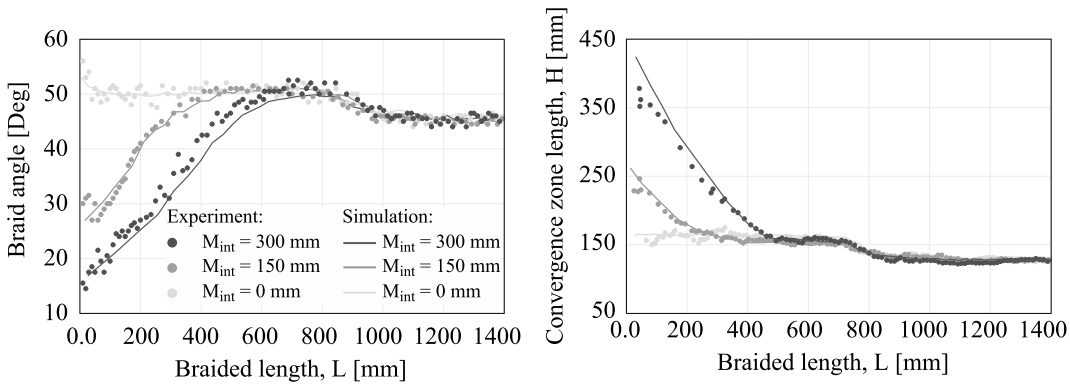

Fig. 14. Experiment and simulation validation for triaxial overbraiding. The anisotropic Howell friction model was used for yarn–yarn contact. M_{int} was varied at 0 mm, 150 mm, and 300 mm.

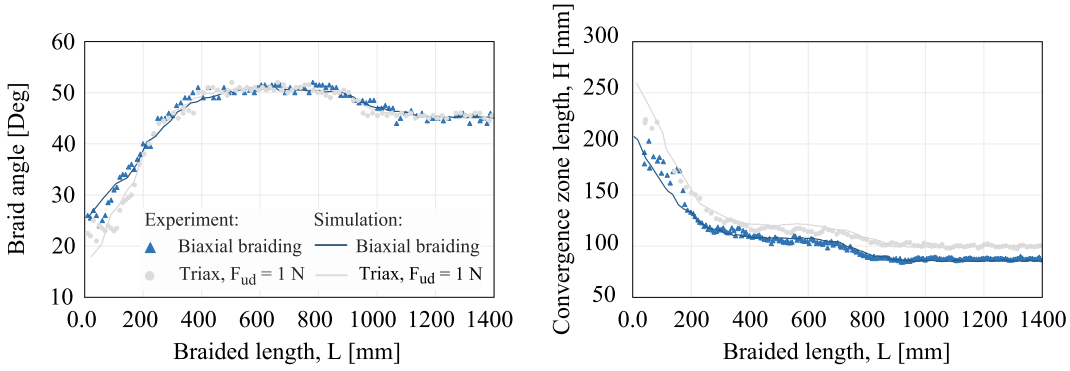

Fig. 15. Experiment and simulation validation using the anisotropic friction model for triaxial and biaxial overbraiding.

and biaxial overbraiding is small. The results show that the triaxial overbraiding simulation has 42 rows of contact in the convergence zone, while the biaxial overbraiding simulation has only 14 rows of contact, leading to a difference of 1344 contact points between the two simulations. This indicates that biaxial overbraiding simulations can effectively predict the braiding angle for triaxial overbraiding with low UD tension, offering the advantage of lower computational cost, as reported in Table 3.

5. Conclusion

This study presented a triaxial overbraiding model that is fast enough to be used for design purposes. The model accounts for mutual interactions between yarns and between yarns and the guide ring. An experimental approach that uses image analysis was developed to measure the convergence zone length and braid angle. The anisotropic Howell friction model with inter-yarn angle and normal force dependence was found to be crucial for accurately predicting the braid angle and convergence zone length during the unsteady state.

The results of this study also suggest that the biaxial overbraiding simulation is a cost-effective and reliable method to simulate triaxial overbraiding with low UD tension, making it a viable alternative to the more computationally expensive triaxial overbraiding simulation. However, it was observed that high UD tensions have a clear effect on the process, emphasizing the importance of utilizing the triaxial overbraiding model in such cases.

Incorporating friction is shown to be valuable when using mandrel shapes with sudden changes in the cross section, or when the process involves changes in take-up speed and spool rotation speed. In such cases, the process shifts from a steady state to an unsteady state, and this transition is influenced by the friction between yarns. On the other hand, the yarn interaction can be omitted for simple mandrel shapes (e.g. cylindrical mandrel) and overbraided under steady state conditions. It is worth noting that friction does affect the initial unsteady state braid angle when using simple mandrel shapes, making it a factor that requires attention.

Further validation should be performed on more complex mandrels, first of all considering the braid angle distribution along the perimeter and length of the mandrel. Further investigation on the influence of guide ring size and shape on both the braid angle and convergence zone length is recommended. In addition to this, the current model does not yet account for jamming or concave mandrels which may lead to fiber bridging. Both phenomena require inclusion of a contact search algorithm and this may significantly increase computational cost. Future extension of this model would include its application in optimization procedures, either through direct optimization or by employing meta-modeling and machine learning techniques.

Table 5
Parameters of the anisotropic friction model for the two pairs of contact used in the overbraiding simulations.

Parameter	T300J - T300J	IM7 - T300J
k_{90} [-]	0.130	0.175
n_k [-]	0.491	0.180
n_n [-]	0.197	0.195

CRediT authorship contribution statement

A.N. Vu: Data curation, Formal analysis, Investigation, Methodology, Software, Validation, Visualization, Writing – original draft. **W.J.B. Grouve:** Conceptualization, Supervision, Writing – review & editing. **L.L. Warnet:** Conceptualization, Supervision, Writing – review & editing. **R. Akkerman:** Conceptualization, Funding acquisition,

Project administration, Resources, Supervision, Writing – review & editing.

Declaration of competing interest

The authors declare that they have no known competing financial interests or personal relationships that could have appeared to influence the work reported in this paper.

Data availability

Data will be made available on request.

Acknowledgments

The authors would like to acknowledge the financial support from Interreg North-West Europe in the framework of the Cobracomp project (Nr. NWE885). The support from the industrial and academic partners of the project is gratefully acknowledged, in particular Eurocarbon B.V. for the supply of testing material and facilitating the experimental work.

References

[1] Kyosev Y. Advances in braiding technology. Woodhead Publishing; 2016.
[2] Branscomb DJ, Beale DG, Broughton R. New directions in braiding. J Eng Fibers Fabrics 2013;11–24.
[3] Gries T, Veit D, Wulfhorst B. Textile technology : An introduction. Hanser; 2014.
[4] Boisse P. Composite reinforcements for optimum performance. Woodhead Publishing; 2011.
[5] Kyosev Y. Recent developments in braiding and narrow weaving. Springer; 2016.
[6] van Ravenhorst JH. Design tools for circular overbraiding of complex mandrels [Ph.D. thesis], Netherlands: University of Twente; 2018.
[7] Kessels JFA, Akkerman R. Prediction of the yarn trajectories on complex braided preforms. Composites A 2002;33(8):1073–81.
[8] van Ravenhorst JH, Akkerman R. Circular braiding take-up speed generation using inverse kinematics. Composites A 2014;64:147–58.
[9] van Ravenhorst JH, Akkerman R. A yarn interaction model for circular braiding. Composites A 2016;81:254–63.
[10] Gondran M, Abdin Y, Gendreau Y, Khameneifar F, Laberge Lebel L. Automated braiding of non-axisymmetric structures using an iterative inverse solution with angle control. Composites A 2021;143:106288.
[11] Monnot P, Lévesque J, Laberge Lebel L. Automated braiding of a complex aircraft fuselage frame using a non-circular braiding model. Composites A 2017;102:48–63.
[12] Vu AN, Grouve WJB, Akkerman R. Modeling of yarn interactions for non-axisymmetric biaxial overbraiding simulations. Composites A 2023;167:107421.
[13] Kyosev Y. Braiding technology of textiles. Woodhead Publishing; 2014.
[14] Ma G, Branscomb DJ, Beale DG. Modeling of the tensioning system on a braiding machine carrier. Mech Mach Theory 2012;47:46–61.
[15] Du GW, Popper P. Analysis of a circular braiding process for complex shapes. J Textile Inst 1994;85(3):316–37.
[16] Ko FK. Braiding. engineered materials handbook, Vol. 1. ASM International; 1987, p. 519.
[17] Pickett AK, Sirtautas J, Erber A. Braiding simulation and prediction of mechanical properties. Appl Compos Mater 2009;16(6):345.
[18] Pickett A, Erber A, von Reden T, Drechsler K. Comparison of analytical and finite element simulation of 2D braiding. Plastics Rubber Composit 2013;38:387–95.
[19] Swery EE, Hans T, Bultez M, Wijaya W, Kelly P, Hinterhölzl R, et al. Complete simulation process chain for the manufacturing of braided composite parts. Composites A 2017;102:378–90.
[20] Sun X, Kawashita LF, Wollmann T, Spitzer S, Langkamp A, Gude M. Experimental and numerical studies on the braiding of carbon fibres over structured end-fittings for the design and manufacture of high performance hybrid shafts. Prod Eng 2018;12(2):215–28.
[21] Heieck F, Kuon C, Miene A, Middendorf P, Herrmann AS. Scatter of mechanical properties of 2D biaxial and triaxial braided reinforced composites and their correlation with visual features. Compos Struct 2023;322:117409.
[22] Ebel C, Mierzwa A, Kind K. Yarn damage during braiding of reinforcement fibers for composites. In: Kyosev Y, editor. Advances in braiding technology. Woodhead publishing series in textiles, Woodhead Publishing; 2016, p. 319–54.
[23] Calba J, Soulat D, Legrand X, Renauld S. Damage investigation on the carbon tows during rewinding and braiding processes. Fibers 2023;11.
[24] Hans T, Cichosz J, Brand M, Hinterhölzl R. Finite element simulation of the braiding process for arbitrary mandrel shapes. Composites A 2015;77:124–32.
[25] www.braidsim.com.
[26] van Ravenhorst J, Akkerman R. Overbraiding simulation. In: Kyosev Y, editor. Advances in braiding technology. Woodhead Publishing; 2016, p. 431–55.
[27] Amontons G. De la Résistance Causée dans les Machines. Mémoires de l'Académie Royale A; 1699, p. 257–82.
[28] Huffington JD, Stout HP. The friction of fibre assemblies. Wear 1960;3(1):26–42.
[29] Cornelissen B, Rietman B, Akkerman R. Frictional behaviour of high performance fibrous tows: Friction experiments. Composites A 2013;44:95–104.
[30] Mulvihill DM, Smerdova O, Sutcliffe MPF. Friction of carbon fibre tows. Composites A 2017;93:185–98.
[31] Chakladar ND, Mandal P, Potluri P. Effects of inter-tow angle and tow size on carbon fibre friction. Composites A 2014;65:115–24.
[32] Tourlonias M, Bueno M-A, Fassi G, Aktas I, Wielhorski Y. Influence of friction angle between carbon single fibres and tows: Experimental analysis and analytical model. Composites A 2019;124:105478.
[33] Vu AN, Grouve WJB, de Rooij MB, Akkerman R. A mesoscopic model for inter-yarn friction. Composit A Appl Sci Manuf 2023. [submitted for publication].
[34] Howell HG, Mazur J. Amontons' law and fibre friction. J. Textile Inst Trans 1953;44(2):T59–69.
[35] Howell HG, Mieszkis KW, Tabor D. Friction in textiles. Nature 2013;184:1765.
[36] Vu AN, Grouve WJB, de Rooij MB, Akkerman R. Supplementary data for the paper: A mesoscopic model for inter-yarn friction. 2023, http://dx.doi.org/10.4121/A36D438A-95B5-440F-9E3D-CB526D2D6562.V1.
[37] Ershov SV, Reimer V, Zastrow T, Kalinin EN, Gries T. Method for measuring the braid angle and its deviation from the specified value in braided preforms using image analysis. Fibre Chem 2022;53:346–54.
[38] Hunt AJ, Carey JP. A machine vision system for the braid angle measurement of tubular braided structures. Textile Res J 2019;89(14):2919–37.